Three-Level Unidirectional Rectifiers under Non-Unity Power Factor Operation and Unbalanced Split DC-Link Loading: Analytical and Experimental Assessment

(Article begins on next page)

10 April 2024
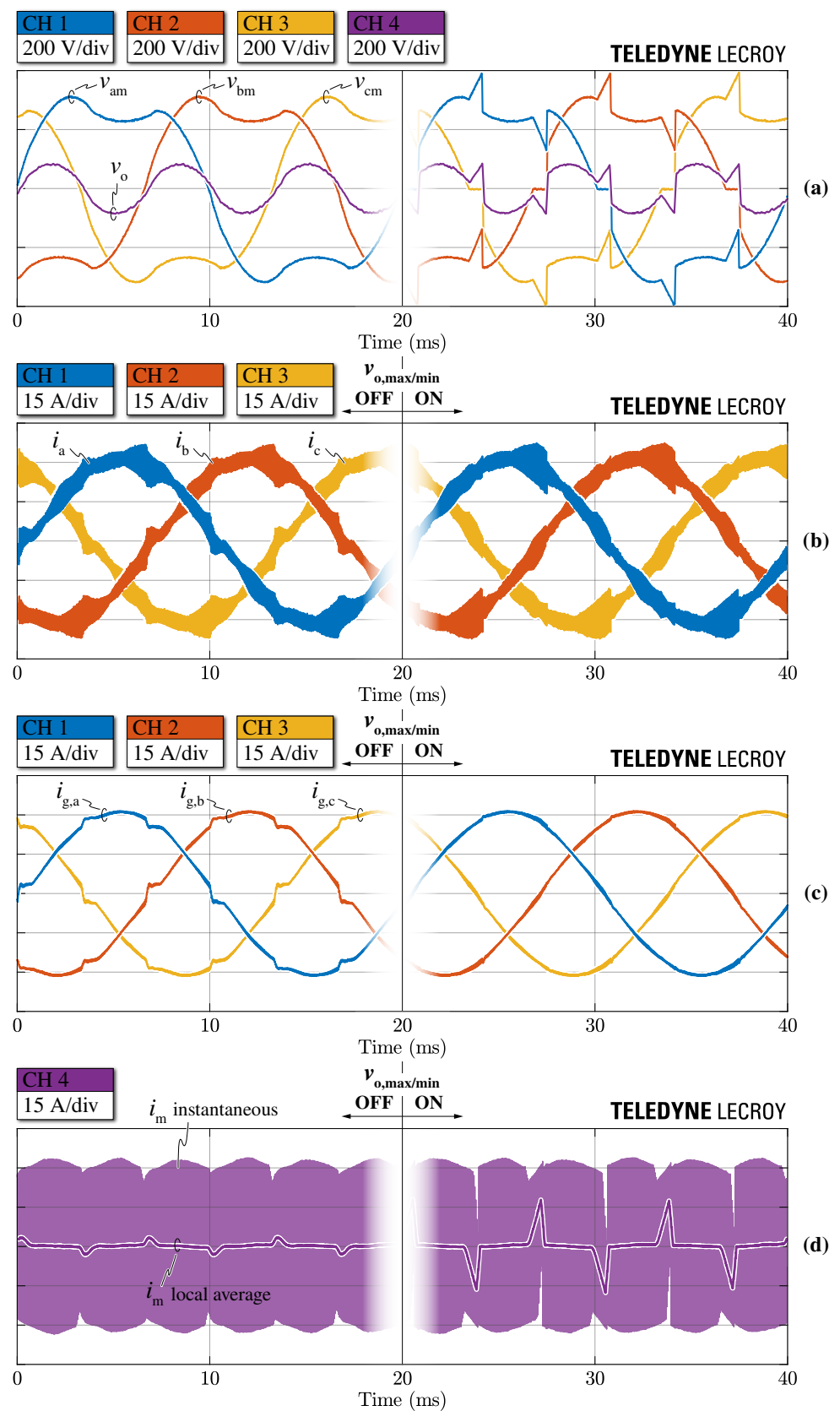
Figure 17. Experimental waveforms in steady-state conditions with $V_{dc} = 800\,\text{V}$, $\varphi = 15°$ and $S = 15\,\text{kVA}$. From top to bottom: (**a**) reference bridge-leg voltages v_{am}, v_{bm}, v_{cm} and zero-sequence voltage v_o (from DAC of the MCU), (**b**) converter-side currents i_{abc}, (**c**) grid-side currents $i_{g,abc}$, (**d**) and mid-point current i_m, with and without the zero-sequence voltage saturation $v_{o,max/min}$.
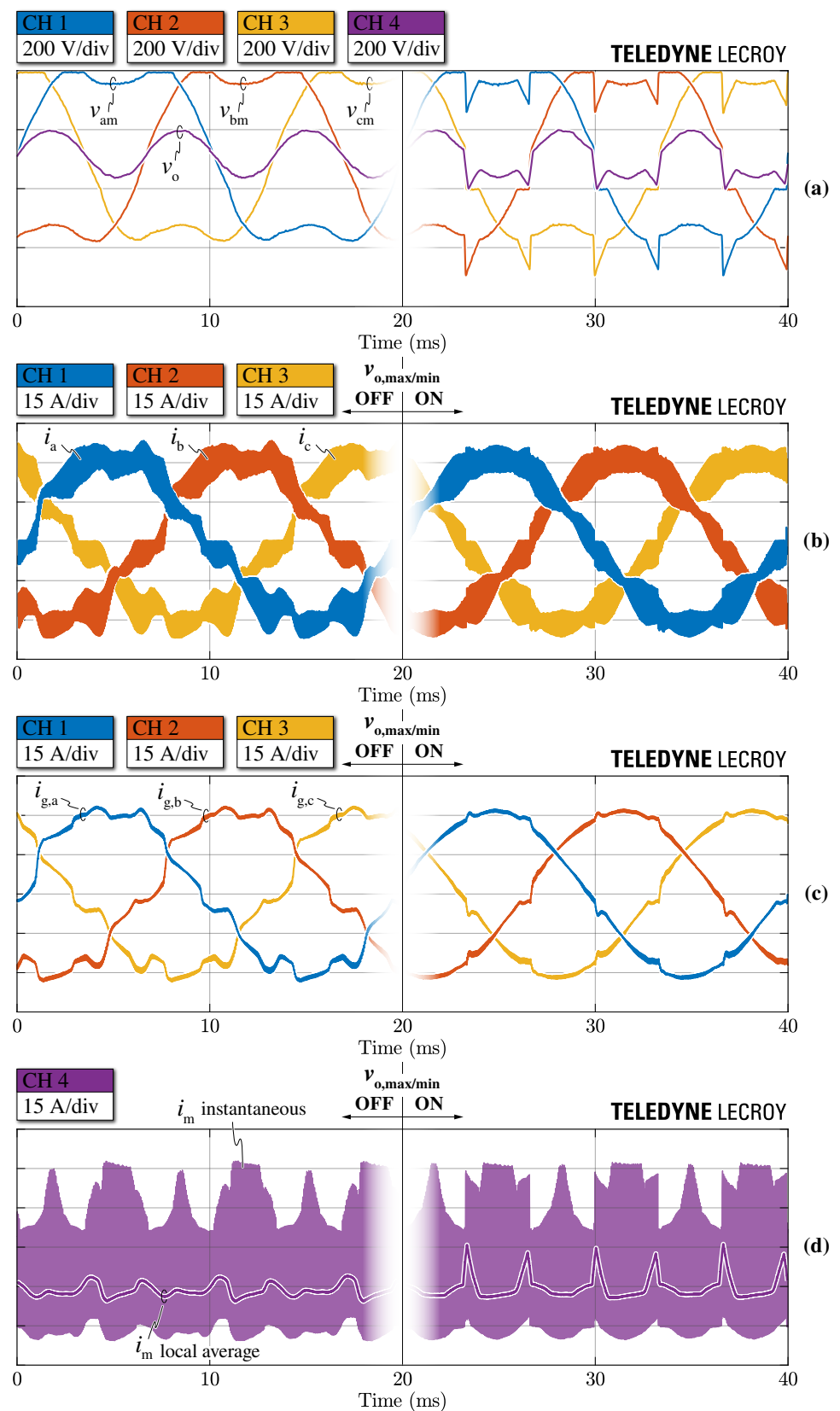
Figure 18. Experimental waveforms in steady-state conditions with $V_{dc} = 800\,\text{V}$, $\varphi = 0$ and $P = 15\,\text{kW}$. A constant zero-sequence voltage component $v_o = 0.15\,{}^{V_{dc}}/2$ is added to $v_{o,3}$ (ZM-PCPWM). From top to bottom: (**a**) reference bridge-leg voltages v_{am}, v_{bm}, v_{cm} and zero-sequence voltage v_o (from DAC of the MCU), (**b**) converter-side currents i_{abc}, (**c**) grid-side currents $i_{g,abc}$, (**d**) and mid-point current i_m, with and without the zero-sequence voltage saturation $v_{o,max/min}$.
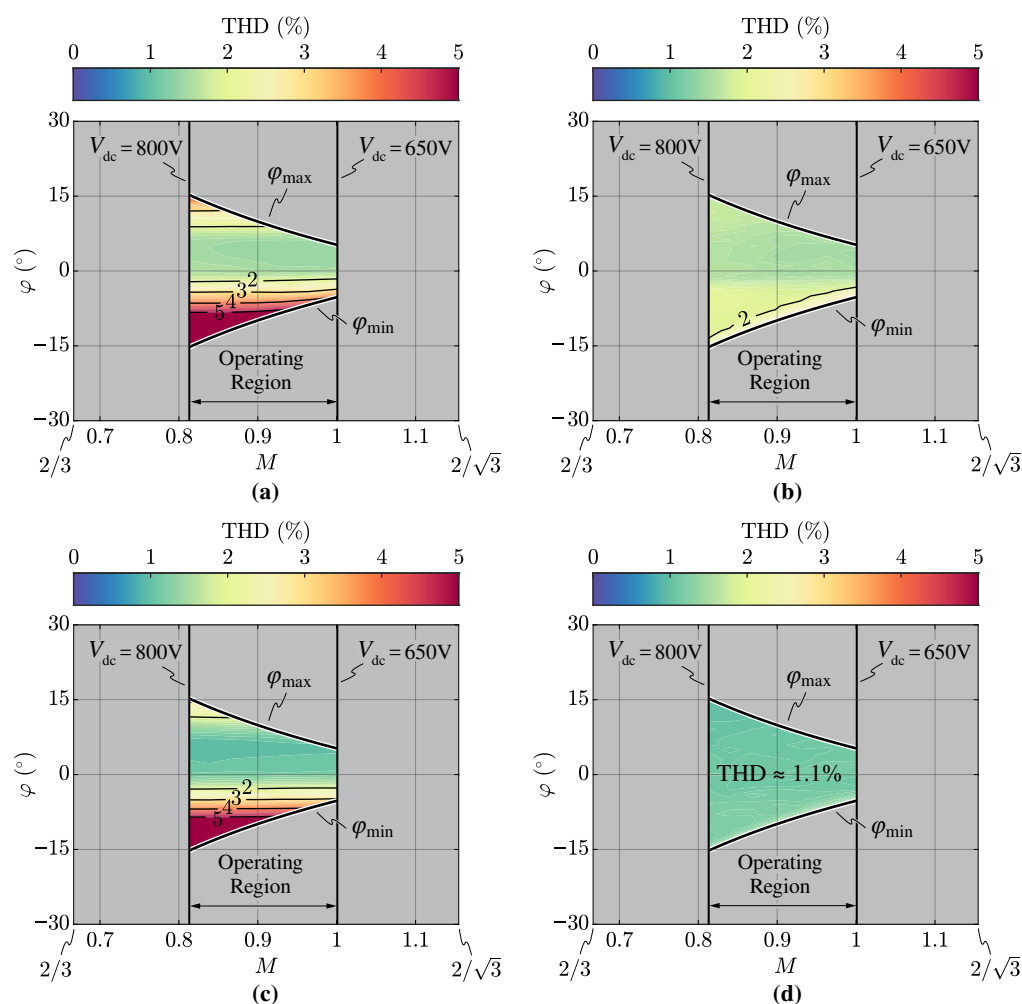
3.2.1. Total Harmonic Distortion (THD)

The grid-side current total harmonic distortion (THD) is defined as

$$\text{THD} = \frac{\sqrt{I_{\text{g,RMS}}^2 - I_{\text{g,1,RMS}}^2}}{I_{\text{g,1,RMS}}} \tag{28}$$

where $I_{\text{g,RMS}}$ is the total RMS value of the grid-side current and $I_{\text{g,1,RMS}}$ is the RMS value of the grid current first harmonic.

The rectifier performance is mapped over the complete modulation index M and converter-side power factor angle φ operating region, both at 50% and 100% of the nominal apparent power (i.e., $S = 30\,\text{kVA}$). The results are shown in Figure 19, where the THD performance obtained with and without $v_{\text{o,max/min}}$ saturation are compared. As expected from Figure 14, the quality of the grid-side current improves at higher load levels, as the zero-crossing distortion is reduced. Moreover, by enforcing the zero-sequence voltage saturation, the THD lies below the conventional 5% limit (i.e., required by grid standards [44]) for all operating points, which is not the case when $v_{\text{o,max/min}}$ is disabled. Finally, it is observed that the THD values are not symmetrical with respect to φ, resulting in worse distortion for $\varphi < 0$ (i.e., capacitive operation). The main explanation resides in the fact that the zero-sequence voltage saturation modifies the current ripple shape and amplitude, leading to a wider DCM operation around the zero-crossings for negative values of φ.

Figure 19. Experimental grid-side current total harmonic distortion (THD) for $S = 15\,\text{kVA}$ (**a,b**) and $S = 30\,\text{kVA}$ (**c,d**). Results without zero-sequence voltage saturation (**a,c**) and with zero-sequence voltage saturation (**b,d**).
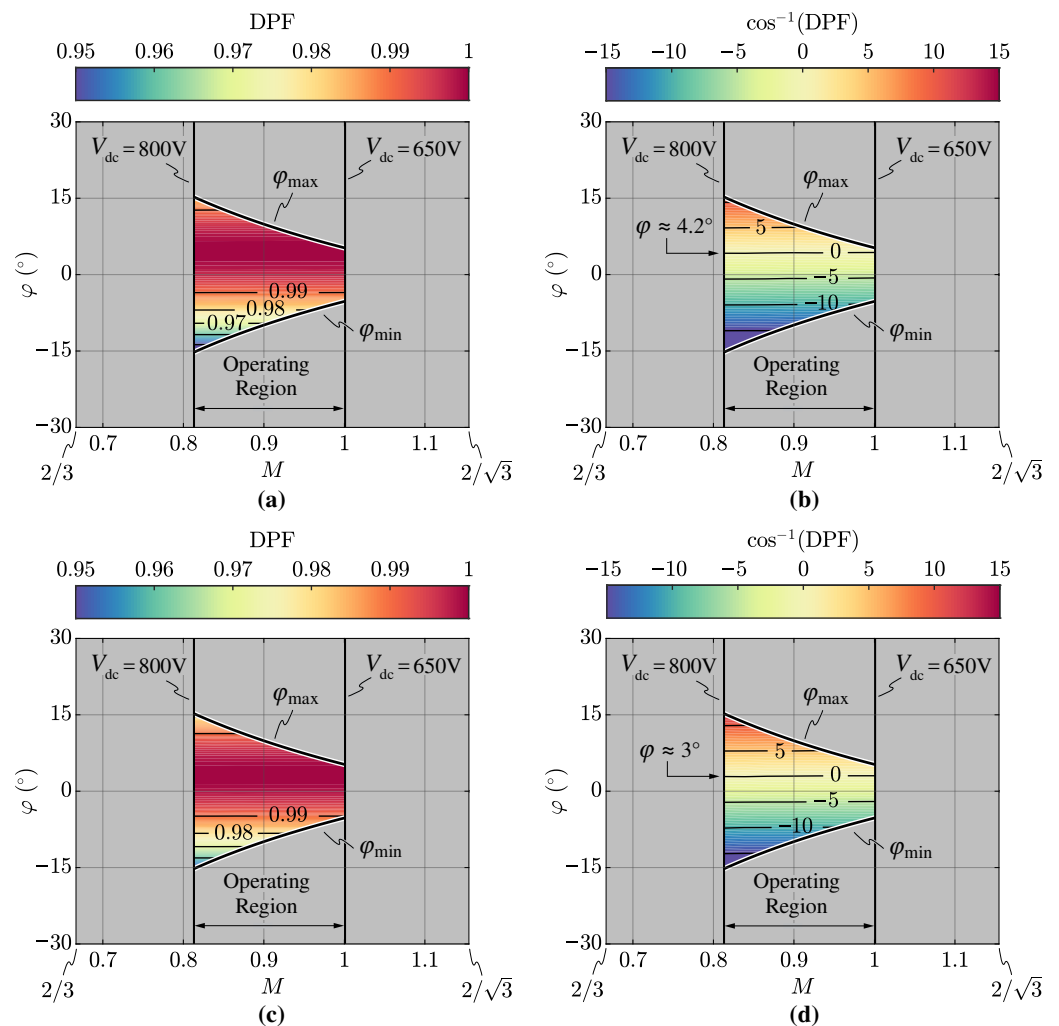
3.2.2. Displacement Power Factor (DPF)

The displacement power factor (DPF) of the rectifier is defined as

$$\text{DPF} = \cos\left(\angle\vec{U} - \angle\vec{I}_g\right) = \frac{P}{S} \tag{29}$$

where $\angle\vec{U}$ and $\angle\vec{I}_g$ are the phase angles of the grid voltage vector (i.e., measured at the PCC) and the grid current vector, respectively. It is worth noting that DPF $\neq \varphi$, as the grid-side converter current also includes the filter capacitor current contribution. The experimental DPF is illustrated in Figure 20a,c for 50% and 100% of the nominal apparent power (i.e., $S = 30\,\text{kVA}$). In both cases, the zero-sequence voltage saturation is enabled.

For a better understanding of the phase-shift between $\vec{U}$ and $\vec{I}_g$, the DPF angle (i.e., $\cos^{-1}(\text{DPF})$) is shown in Figure 20b,d, where a positive value indicates a lagging power factor (i.e., inductive behavior) and a negative value indicates a leading power factor (i.e., capacitive behavior). It can be observed that the current flowing into the filter capacitor C_f is completely compensated for $\varphi \approx 4.2°$ at 50% of the rated power and $\varphi \approx 3°$ at 100% of the rated power, as expected from basic theoretical considerations.

Figure 20. Experimental displacement power factor (DPF) (**a**,**c**) and DPF angle (**b**,**d**) for $S = 15\,\text{kVA}$ (**a**,**b**) and $S = 30\,\text{kVA}$ (**c**,**d**). The current flowing into the filter capacitor C_f is completely compensated for $\varphi \approx 4.2°$ in (**b**) and $\varphi \approx 3°$ in (**d**).

3.2.3. Maximum Mid-Point Current ($I_{m,max}$)

The maximum DC-link mid-point current capability of the rectifier ($I_{m,max}$) is assessed experimentally by operating the converter at 50% of the rated apparent power (i.e., $S = 15\,\text{kVA}$) and injecting a zero-sequence voltage equal to $v_{o,min}$. The results are illustrated in Figure 8b in Section 2.5, where they are normalized with respect to the converter-side peak current value I. It is observed that the theoretical and the experimental results are in close agreement, achieving a maximum deviation of 5% over the complete operating range of the rectifier. Therefore, the analytical $I_{m,max}$ formulas derived in Appendix A can be considered successfully verified.

3.2.4. Minimum Mid-Point Charge Ripple ($\Delta Q_{m,pp,min}$)

The minimum DC-link mid-point peak-to-peak charge ripple $\Delta Q_{m,pp,min}$ is assessed experimentally by operating the converter at 100% of the rated apparent power (i.e., $S = 30\,\text{kVA}$), injecting the zero-sequence voltage component $v_{o,3}$ defined by ZMPCPWM and saturating it according to the $v_{o,max/min}$ limits. In particular, the mid-point charge is obtained in post-processing as the integral of the measured mid-point current i_m. The results are illustrated in Figure 10b in Section 2.6, where they are normalized with respect to the converter-side peak phase current I and three-times the grid frequency $3f$. Additionally in this case, the theoretical and the experimental results are in close agreement; however, the value $\Delta Q_{m,pp,min}$ obtained experimentally does not reach 0 for $\varphi = 0$. This is mainly due to the converter-side current not being perfectly sinusoidal, as it features a slight zero-crossing distortion that yields a non-zero mid-point current local average (see Figure 15). Nevertheless, $\Delta Q_{m,pp,min} = 0$ can never be achieved in practice, as the switching-frequency mid-point current ripple (i.e., neglected in the theoretical model) yields a non-zero charge ripple: theoretical and experimental results at $\varphi = 0$ would only coincide for $f_{sw} = \infty$. Overall, the analytical $\Delta Q_{m,pp,min}$ formula derived in Appendix B can be considered successfully verified, achieving best estimation accuracy for systems with $f_{sw} \gg f$ (i.e., with high pulse ratios).

4. Conclusions

This paper has presented a comprehensive analysis and performance assessment of three-phase three-level unidirectional rectifiers under non-unity power factor operation and unbalanced split DC-link loading.

The complete analysis applies to all three-level unidirectional rectifiers and thus features a wide range of applications, e.g., active front ends for the supply of variable-speed drives, uninterruptible power supply systems, battery chargers, data centers and high-power DC loads. In particular, the ability to operate under non-unity power factor is becoming a desired feature of modern rectifiers, as distribution system operators worldwide are starting to charge end consumers for the excess reactive energy injected/withdrawn into/from the grid. In this scenario, properly controlled unidirectional rectifiers could support the reactive energy flows and potentially substitute traditional power factor correction capacitor banks, without requiring new or additional hardware. Furthermore, the ability to operate under unbalanced split DC-link loading is necessary when separate loads are connected to the rectifier DC-link halves, which is typically the case for modular high-power converters (e.g., the DC/DC stage of electric vehicle DC fast chargers).

Therefore, this paper has focused on analyzing, improving and extending the operation of three-phase three-level unidirectional rectifiers. First, the operational basics of three-level rectifiers have been recalled and the theoretical operating limits of the converter in terms of zero-sequence voltage, modulation index, power factor angle, DC-link mid-point current and minimum DC-link mid-point charge ripple have been derived. A unified carrier-based pulse-width modulation (PWM) approach aiming for the undistorted operation of the rectifier across all feasible operating conditions has been proposed, de facto enabling the converter operation under non-unity power factor and unbalanced split-DC-link loading. This approach, uniquely based on restraining (i.e., saturating) the zero-sequence voltage within its feasible limits, has been described in detail and its effects

on the DC-link mid-point current generation have been investigated. Furthermore, novel analytical expressions have been derived in the Appendix, defining the rectifier maximum mid-point current capability (i.e., directly linked to the converter DC-link load unbalance) and the minimum peak-to-peak DC-link mid-point charge ripple (i.e., allowing for the straightforward sizing of the DC-link capacitance value) over the complete converter operating region. Finally, the theoretical analysis has been successfully verified on a digitally controlled 30 kW T-type rectifier prototype operating at 20 kHz. The input phase current total harmonic distortion (THD), the maximum mid-point current capability and the minimum mid-point peak-to-peak charge ripple have been experimentally assessed across all rectifier operating points, demonstrating excellent performance and a high-level of agreement with the analytical predictions.

Appendix A. Analytical Derivation of the Mid-Point Current Limits

The boundaries of the mid-point current periodical average I_m can be derived averaging the maximum and minimum feasible envelopes of i_m along the grid period, i.e., integrating (24) over $2\pi/3$. In particular, being the integrals of $i_{m,max}$ and $i_{m,min}$ identical but with opposite sign, the I_m limits are symmetrical:

$$I_{m,max} = -I_{m,min} = -\frac{3}{\pi\,V_{dc}} \int\limits_0^{2\pi/3} \left[\sum_{x=a,b,c} v_x\,|i_x| + v_{o,min} \sum_{x=a,b,c} |i_x| \right] d\vartheta. \tag{A1}$$
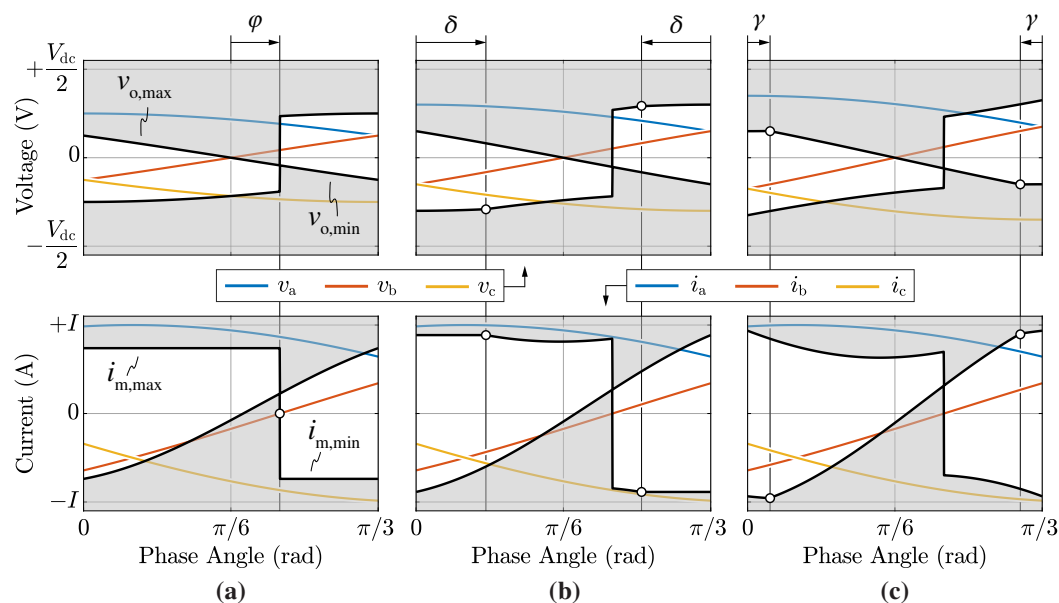
Figure A1. Zero-sequence voltage limits $v_{o,max}$, $v_{o,min}$ and mid-point current local average limits $i_{m,max}$, $i_{m,min}$ for (**a**) $M = 0.5$ (region ①), (**b**) $M = 0.6$ (region ②) and (**c**) $M = 0.7$ (region ③) assuming $\varphi = 10°$. The focus is on $0 \leq \vartheta \leq \pi/3$ to highlight the most relevant angle definitions for the analytical calculations (i.e., φ, δ, γ).

Due to the $2\pi/3$ periodicity of the first term, its integral is null, thus resulting in

$$I_{\text{m,max}} = -\frac{3}{\pi\,V_{\text{dc}}} \int_0^{2\pi/3} v_{\text{o,min}}\,(|i_{\text{a}}| + |i_{\text{b}}| + |i_{\text{c}}|)\,\mathrm{d}\vartheta. \tag{A2}$$

To ease the solution of (A2), it is worth observing that $i_{\text{m,max}}$ for $0 \le \vartheta \le \pi/3$ is equal to $-i_{\text{min}}$ for $\pi/3 \le \vartheta \le 2\pi/3$ (see Figures 6 and 7). Therefore, the integration interval may be restricted to $\vartheta \in [0,\,\pi/3]$ by considering both maximum and minimum i_{m} envelopes. A highlight of the waveforms within the selected integration interval is provided in Figure A1.

Therefore, leveraging the $v_{\text{o,min}}$ definition and the signs of i_{a}, i_{b}, i_{c} inside the considered averaging window, different $I_{\text{m,max}}$ expressions are obtained depending on the value of the modulation index. In particular, three main regions can be defined, as illustrated in Figure A2: region ① with $M < 1/\sqrt{3}$, region ② with $1/\sqrt{3} \le M \le 2/3$ (i.e., the transition region) and region ③ with $M > 2/3$. The current and voltage waveforms for regions ①, ② and ③ are reported in Figure A1a–c, respectively.
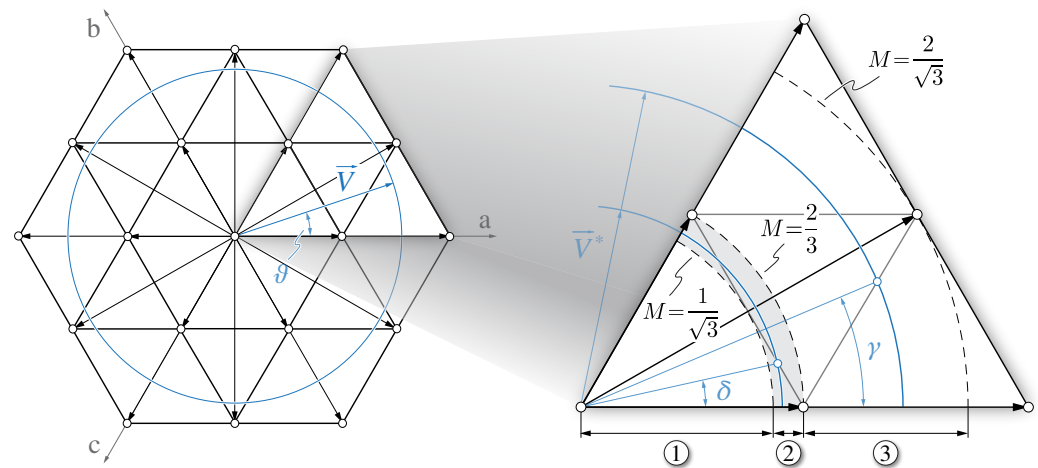
Figure A2. Overview of the modulation index regions ①, ② and ③ on the space vector diagram, focusing on $0 \le \vartheta \le \pi/3$. The transition region ② is highlighted in grey and the most significant angle definitions for the analytical calculations are indicated (i.e., ϑ, δ, γ).

The expressions of $I_{\text{m,max}}$ are therefore:

$$I_{\text{m,max},①} = \frac{6}{\pi\,V_{\text{dc}}}\left[\int_0^{\pi/6+\varphi} i_{\text{a}}\,v_{\text{a}}\,\mathrm{d}\vartheta - \int_{\pi/6+\varphi}^{\pi/3} i_{\text{c}}\,v_{\text{b}}\,\mathrm{d}\vartheta - \int_0^{\pi/6+\varphi} i_{\text{a}}\,v_{\text{b}}\,\mathrm{d}\vartheta + \int_{\pi/6+\varphi}^{\pi/3} i_{\text{c}}\,v_{\text{c}}\,\mathrm{d}\vartheta \right], \tag{A3}$$

valid for $M < 1/\sqrt{3}$,

$$I_{\text{m,max},②} = \frac{6}{\pi\,V_{\text{dc}}}\left[-\int_0^{\pi/6+\varphi} i_{\text{a}}\,v_{\text{b}}\,\mathrm{d}\vartheta - \int_{\pi/6+\varphi}^{\pi/3-\delta} i_{\text{c}}\left(\frac{V_{\text{dc}}}{2} - v_{\text{a}}\right)\mathrm{d}\vartheta + \int_{\pi/3-\delta}^{\pi/3} i_{\text{c}}\,v_{\text{c}}\,\mathrm{d}\vartheta + \right.$$
$$\left. + \int_0^{\delta} i_{\text{a}}\,v_{\text{a}}\,\mathrm{d}\vartheta + \int_{\delta}^{\pi/6+\varphi} i_{\text{a}}\left(\frac{V_{\text{dc}}}{2} + v_{\text{c}}\right)\mathrm{d}\vartheta - \int_{\pi/6+\varphi}^{\pi/3} i_{\text{c}}\,v_{\text{b}}\,\mathrm{d}\vartheta \right], \tag{A4}$$

valid for $1/\sqrt{3} \leq M \leq 2/3$, and

$$
I_{m,max,\text{③}} = \frac{6}{\pi V_{dc}} \left[\int_{0}^{\pi/6+\varphi} i_a \left(\frac{V_{dc}}{2} + v_c \right) d\vartheta - \int_{\pi/6+\varphi}^{\pi/3-\gamma} i_c v_b \, d\vartheta - \int_{\pi/3-\gamma}^{\pi/3} i_c \left(\frac{V_{dc}}{2} + v_c \right) d\vartheta + \right.
$$
$$
\left. + \int_{0}^{\gamma} i_a \left(\frac{V_{dc}}{2} - v_a \right) d\vartheta - \int_{\gamma}^{\pi/6+\varphi} i_a v_b \, d\vartheta - \int_{\pi/6+\varphi}^{\pi/3} i_c \left(\frac{V_{dc}}{2} - v_a \right) d\vartheta \right], \quad (A5)
$$

valid for $M > 2/3$. The angles δ, γ are graphically illustrated in Figures A1 and A2, and their expression is obtained by setting $v_a = v_c + V_{dc}/2$ and $v_a - V_{dc}/2 = v_b$, respectively, as

$$
\delta = \frac{\pi}{6} - \cos^{-1}\left(\frac{1}{\sqrt{3}M} \right) \qquad \frac{1}{\sqrt{3}} \leq M \leq \frac{2}{3}, \tag{A6}
$$

$$
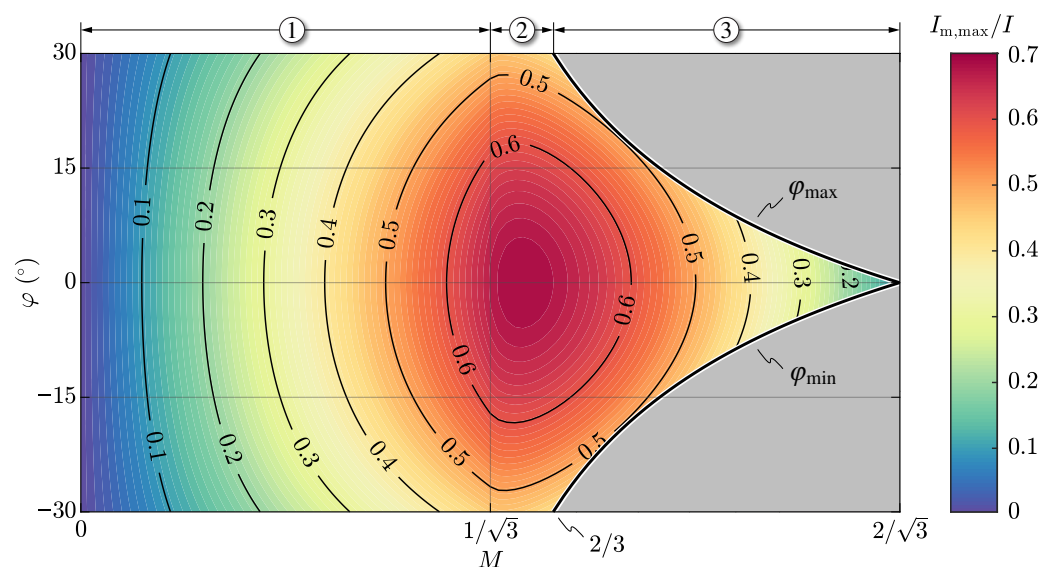\gamma = \frac{\pi}{3} - \sin^{-1}\left(\frac{1}{\sqrt{3}M} \right) \qquad M \geq \frac{2}{3}. \tag{A7}
$$

Finally, substituting (3), (5), (A6), (A7) into (A3)–(A5) and solving the integral terms, the following analytical expressions are obtained:

$$
I_{m,max,\text{①}} = \frac{3}{\pi} I \frac{M}{4} \cos\varphi \left(\pi + \sqrt{3} - 2\sqrt{3} \, \varphi \tan\varphi \right) \tag{A8}
$$

valid for $M < 1/\sqrt{3}$ and

$$
I_{m,max,\text{②}} = I_{m,max,\text{③}} = \frac{3}{\pi} I \left[1 + \frac{1}{2M} \cos\varphi \left(\sqrt{3M^2 - 1} - \frac{1}{\sqrt{3}} \right) + \right.
$$
$$
\left. + \frac{M}{2} \cos\varphi \left(3 \sin^{-1}\left(\frac{1}{\sqrt{3}M} \right) - \pi - \frac{\sqrt{3}}{2} - 2\sqrt{3} \, \varphi \tan\varphi \right) \right] \tag{A9}
$$

valid for $M > 1/\sqrt{3}$. Expressions (A8) and (A9) are graphically illustrated in Figure A3, where the modulation index regions ①, ② and ③ are also indicated.


Figure A3. Maximum mid-point current periodical average $I_{m,max}$ (i.e., normalized with respect to the peak phase current I) as a function of the modulation index M and the converter-side power factor angle φ. The three modulation index regions ①, ② and ③ are indicated.

It is worth noting that this analytical derivation extends the approach reported in [16], where the mid-point current periodical average limits are derived uniquely for $\varphi = 0$.

Appendix B. Analytical Derivation of the Minimum Mid-Point Charge Ripple

To identify the minimum value of DC-link mid-point peak-to-peak charge ripple $\Delta Q_{m,pp}$, the zero mid-point current modulation (ZMPCPWM) is considered, therefore the third-harmonic zero-sequence voltage reported in (26) is added to the phase voltage references. Figure A4 shows the zero-sequence voltage v_o waveform and the mid-point current local average i_m waveform for $M = 0.8$ and $\varphi = 15°$. In particular, it is observed that the zero-sequence voltage saturation occurring for $\varphi \neq 0$ causes a deviation of the mid-point current average, which in turn leads to a non-zero $\Delta Q_{m,pp}$.
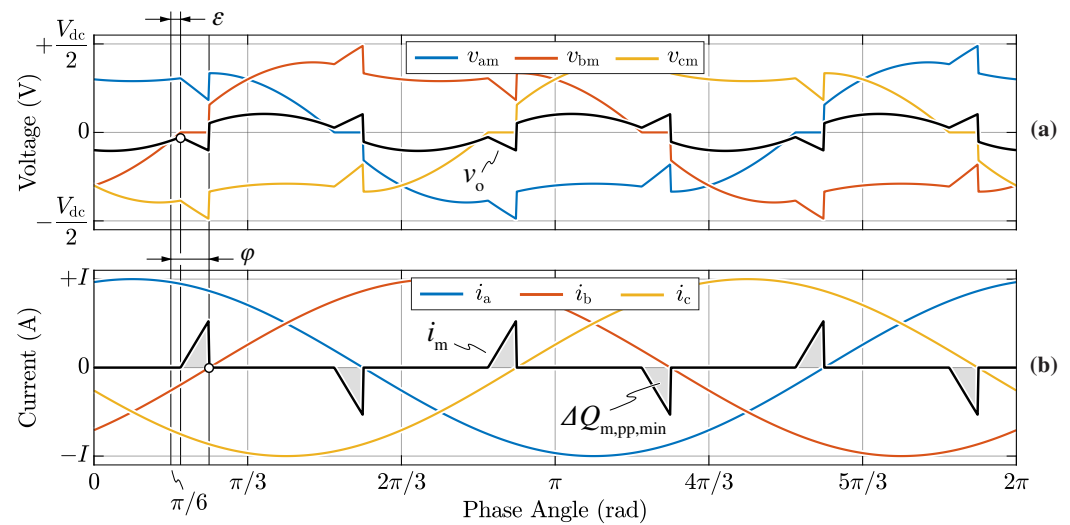
Figure A4. Zero-sequence voltage v_o (**a**) and mid-point current local average i_m (**b**) for $M = 0.8$ (region ③) and $\varphi = 15°$. Zero mid-point modulation (ZMPCPWM) is adopted. The most relevant angle definitions for the analytical calculations (i.e., φ, ε) are indicated.

Figure A4 also shows that when ZMPCPWM is adopted, $i_m \geq 0$ within $0 \leq \vartheta \leq \pi/3$, thus leading to a simplified expression of the mid-point charge ripple:

$$\Delta Q_{m,pp} = \frac{1}{2\pi f} \int_0^{\pi/3} i_m \, d\vartheta, \tag{A10}$$

Therefore, due to i_m being null for most of the period, the minimum $\Delta Q_{m,pp}$ can be calculated by restricting the integration interval to

$$\Delta Q_{m,pp,min} = \frac{1}{2\pi f} \int_{\pi/6+\varepsilon}^{\pi/6+\varphi} i_m \, d\vartheta = -\frac{1}{\pi f V_{dc}} \int_{\pi/6+\varepsilon}^{\pi/6+\varphi} \left[\sum_{x=a,b,c} v_x |i_x| + v_{o,min} \sum_{x=a,b,c} |i_x| \right] d\vartheta, \tag{A11}$$

where i_m has been substituted with (16), $v_o = v_{o,min}$ within $\pi/6 + \varepsilon \leq \vartheta \leq \pi/6 + \varphi$, and ε is obtained by setting $v_{o,3} = -v_b$, as
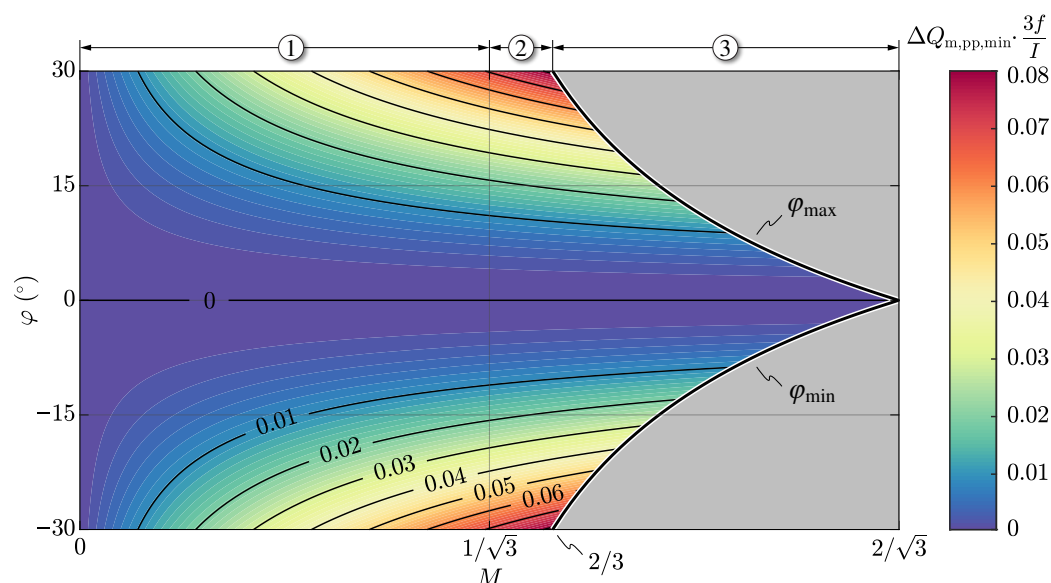
$$\varepsilon = \frac{1}{2} \left[\varphi - \frac{\pi}{2} + \cos^{-1} \left(\frac{1}{2} \sin \varphi \right) \right]. \tag{A12}$$

Finally, substituting (3), (5), (A12) into (A11) and solving the integral terms, the following analytical expression is obtained:

$$\Delta Q_{m,pp,min} = \frac{\sqrt{3}}{8\pi f} IM \left[\sqrt{4 - \sin^2\varphi} - 2\cos\varphi - \sin\varphi \left(\cos^{-1}\left(\frac{\sin\varphi}{2}\right) - \frac{\pi}{2} - \varphi \right) \right], \quad (A13)$$

valid for the complete modulation index range $0 \leq M \leq 2/\sqrt{3}$. Expression (A13) is illustrated in normalized form in Figure A5, where the modulation index regions ①, ② and ③ are also indicated.

Figure A5. Minimum DC-link mid-point charge ripple $\Delta Q_{m,pp}$ (i.e., normalized with respect to the peak phase current I and three-times the grid frequency $3f$) as a function of the modulation index M and the converter-side power factor angle φ. The three modulation index regions ①, ② and ③ are indicated.

References

1. Kolar, J.W.; Friedli, T. The Essence of Three-Phase PFC Rectifier Systems—Part I. *IEEE Trans. Power Electron.* **2013**, *28*, 176–198. [CrossRef]
2. Friedli, T.; Hartmann, M.; Kolar, J.W. The Essence of Three-Phase PFC Rectifier Systems—Part II. *IEEE Trans. Power Electron.* **2014**, *29*,
3. Teichmann, R.; Bernet, S. A Comparison of Three-Level Converters versus Two-Level Converters for Low-Voltage Drives, Traction, and Utility Applications. *IEEE Trans. Ind. Appl.* **2005**, *41*, 855–865. [CrossRef]
4. Schweizer, M.; Friedli, T.; Kolar, J.W. Comparative Evaluation of Advanced Three-Phase Three-Level Inverter/Converter Topologies Against Two-Level Systems. *IEEE Trans. Ind. Electron.* **2013**, *60*, 5515–5527. [CrossRef]
5. Cittanti, D.; Guacci, M.; Mirić, S.; Bojoi, R.; Kolar, J.W. Comparative Evaluation of 800V DC-Link Three-Phase Two/Three-Level SiC Inverter Concepts for Next-Generation Variable Speed Drives. In Proceedings of the International Conference on Electrical Machines and Systems (ICEMS), Hamamatsu, Japan, 24–27 November 2020; pp. 1699–1704. [CrossRef]
6. Anderson, J.A.; Zulauf, G.; Kolar, J.W.; Deboy, G. New Figure-of-Merit Combining Semiconductor and Multi-Level Converter Properties. *IEEE Open J. Power Electron.* **2020**, *1*, 322–338. [CrossRef]
7. Kolar, J.; Drofenik, U.; Zach, F. Current Handling Capability of the Neutral Point of a Three-Phase/Switch/Level Boost-Type PWM (VIENNA) Rectifier. In Proceedings of the 27th Annual IEEE Power Electronics Specialists Conference (PESC), Baveno, Italy, 23–27 June 1996; Volume 2, pp. 1329–1336. [CrossRef]
8. Kolar, J.W.; Drofenik, U.; Zach, F.C. On the Interdependence of AC-Side and DC-Side Optimum Control of Three-Phase Neutral-Point-Clamped (Three-Level) PWM Rectifier Systems. In Proceedings of the International Power Electronics and Motion Control Conference (PEMC), Budapest, Hungary, 2–4 September 1996.
9. Kolar, J.; Zach, F. A Novel Three-Phase Utility Interface Minimizing Line Current Harmonics of High-Power Telecommunications Rectifier Modules. *IEEE Trans. Ind. Electron.* **1997**, *44*, 456–467. [CrossRef]

10. Ogasawara, S.; Akagi, H. Analysis of Variation of Neutral Point Potential in Neutral-Point-Clamped Voltage Source PWM Inverters. In Proceedings of the IEEE Industry Applications Conference, Toronto, ON, Canada, 2–8 October 1993; pp. 965–970. [CrossRef]

11. Cittanti, D.; Gregorio, M.; Armando, E.; Bojoi, R. Digital Multi-Loop Control of an LLC Resonant Converter for Electric Vehicle DC Fast Charging. In Proceedings of the IEEE Energy Conversion Congress and Exposition (ECCE), Detroit, MI, USA, 11–15 October 2020; pp. 4423–4430. [CrossRef]

12. Cittanti, D.; Vico, E.; Gregorio, M.; Mandrile, F.; Bojoi, R. Iterative Design of a 60 kW All-Si Modular LLC Converter for Electric Vehicle Ultra-Fast Charging. In Proceedings of the AEIT International Conference of Electrical and Electronic Technologies for Automotive (AEIT AUTOMOTIVE), Turin, Italy, 18–20 November 2020. [CrossRef]

13. Mandrile, F.; Cittanti, D.; Mallemaci, V.; Bojoi, R. Electric Vehicle Ultra-Fast Battery Chargers: A Boost for Power System Stability? *World Electr. Veh. J.* **2021**, *12*, 16. [CrossRef]

14. Lai, R.; Wang, F.; Burgos, R.; Boroyevich, D.; Jiang, D.; Zhang, D. Average Modeling and Control Design for VIENNA-Type Rectifiers Considering the DC-Link Voltage Balance. *IEEE Trans. Power Electron.* **2009**, *24*, 2509–2522. [CrossRef]

15. Leibl, M. Three-Phase PFC Rectifier and High-Voltage Generator for X-ray Systems. Ph.D. Thesis, ETH Zurich, Zurich, Switzerland, 2017. [CrossRef]

16. Cittanti, D.; Gregorio, M.; Bossotto, E.; Mandrile, F.; Bojoi, R. Full Digital Control and Multi-Loop Tuning of a Three-Level T-Type Rectifier for Electric Vehicle Ultra-Fast Battery Chargers. *Electronics* **2021**, *10*, 1453. [CrossRef]

17. Liserre, M.; Blaabjerg, F.; Hansen, S. Design and Control of an LCL-Filter-Based Three-Phase Active Rectifier. *IEEE Trans. Ind. Appl.* **2005**, *41*, 1281–1291. [CrossRef]

18. Cittanti, D.; Mandrile, F.; Bojoi, R. Optimal Design of Grid-Side LCL Filters for Electric Vehicle Ultra-Fast Battery Chargers. In Proceedings of the International Universities Power Engineering Conference (UPEC), Turin, Italy, 1–4 September 2020. [CrossRef]

19. Cittanti, D.; Bojoi, R. Modulation Strategy Assessment for 3-Level Unidirectional Rectifiers in Electric Vehicle Ultra-Fast Charging Applications. In Proceedings of the AEIT International Conference of Electrical and Electronic Technologies for Automotive (AEIT AUTOMOTIVE), Turin, Italy, 18–20 November 2020. [CrossRef]

20. European Union Agency for the Cooperation of Energy Regulators (ACER). Report on Distribution Tariff Methodologies in Europe. 2021. Available online: https://documents.acer.europa.eu/Official_documents/Acts_of_the_Agency/Publication/ACE (accessed on 14 August 2021).

21. Leibl, M.; Kolar, J.W.; Deuringer, J. Sinusoidal Input Current Discontinuous Conduction Mode Control of the VIENNA Rectifier. *IEEE Trans. Power Electron.* **2017**, *32*, 8800–8812. [CrossRef]

22. Lee, J.S.; Lee, K.B. A Novel Carrier-Based PWM Method for Vienna Rectifier With a Variable Power Factor. *IEEE Trans. Ind. Electron.* **2016**, *63*, 3–12. [CrossRef]

23. Wang, F.; Teng, Y.; Yuan, Z.; Xu, J. A Maximum Power Factor of Control Algorithms of Three-Level Vienna Rectifier without Current Distortion at Current Zero-Crossing Point. In Proceedings of the 2016 IEEE 8th International Power Electronics and Motion Control Conference (IPEMC-ECCE Asia), Hefei, China, 22–26 May 2016; pp. 2325–2331. [CrossRef]

24. Hu, W.; Yu, A.; Lyu, J.; Ding, H.; Lyu, J. Research on Reducing the Input Current Distortion based on PWM Method for Vienna Rectifier with LCL Filter. In Proceedings of the 2017 Chinese Automation Congress (CAC), Jinan, China, 20–22 October 2017; pp. 6634–6639. [CrossRef]

25. Xu, H.; Yao, W.; Shao, S. Improved SVPWM Schemes for Vienna Rectifiers without Current Distortion. In Proceedings of the 2017 IEEE Energy Conversion Congress and Exposition (ECCE), Cincinnati, OH, USA, 1–5 October 2017; pp. 3410–3414. [CrossRef]

26. Molligoda, D.A.; Pou, J.; Gajanayake, C.; Gupta, A. Analysis of the Vienna Rectifier under Nonunity Power Factor Operation. In Proceedings of the 2018 Asian Conference on Energy, Power and Transportation Electrification (ACEPT), Singapore, 30 October–2 November 2018; pp. 1–7. [CrossRef]

27. Molligoda, D.A.; Pou, J.; Ceballos, S.; Satpathi, K.; Sasongko, F.; Gajanayake, C.J.; Gupta, A.K. Current Distortion Mitigation in Grid-Connected Vienna Rectifier During Nonunity Power Factor Operation. In Proceedings of the IECON 2020 The 46th Annual Conference of the IEEE Industrial Electronics Society, Singapore, 18–21 October 2020; pp. 4085–4090. [CrossRef]

28. Burgos, R.; Lai, R.; Pei, Y.; Wang, F.; Boroyevich, D.; Pou, J. Space Vector Modulator for Vienna-Type RectifiersBased on the Equivalence BetweenTwo- and Three-Level Converters: A Carrier-Based Implementation. *IEEE Trans. Power Electron.* **2008**, *23*, 1888–1898. [CrossRef]

29. Ding, W.; Zhang, C.; Gao, F.; Duan, B.; Qiu, H. A Zero-Sequence Component Injection Modulation Method With Compensation for Current Harmonic Mitigation of a Vienna Rectifier. *IEEE Trans. Power Electron.* **2019**, *34*, 801–814. [CrossRef]

30. Celanovic, N.; Boroyevich, D. A comprehensive study of neutral-point voltage balancing problem in three-level neutral-point-clamped voltage source PWM inverters. *IEEE Trans. Power Electron.* **2000**, *15*, 242–249. [CrossRef]

31. Pou, J.; Pindado, R.; Boroyevich, D.; Rodriguez, P. Evaluation of the low-frequency neutral-point voltage oscillations in the three-level inverter. *IEEE Trans. Ind. Electron.* **2005**, *52*, 1582–1588. [CrossRef]

32. Wang, C.; Li, Y. Analysis and Calculation of Zero-Sequence Voltage Considering Neutral-Point Potential Balancing in Three-Level NPC Converters. *IEEE Trans. Ind. Electron.* **2010**, *57*, 2262–2271. [CrossRef]

33. Wang, J.; Gui, Z.; Wang, P.; Wang, J.; Jiang, W. A Carrier-Based Modulation With Planned Zero Sequence Voltage Injection to Control Neutral Point Voltage for Three-Level Inverter. *IEEE Access* **2020**, *8*, 64799–64809. [CrossRef]

34. Chen, F.; Qiao, W.; Wang, H.; Qu, L. A Simple Zero-Sequence Voltage Injection Method for Carrier-Based Pulsewidth Modulation of the Three-Level NPC Inverter. *IEEE J. Emerg. Sel. Top. Power Electron.* **2021**, *9*, 4687–4699. [CrossRef]

35. Zhao, W.; Ruan, X.; Yang, D.; Chen, X.; Jia, L. Neutral Point Voltage Ripple Suppression for a Three-Phase Four-Wire Inverter With an Independently Controlled Neutral Module. *IEEE Trans. Ind. Electron.* **2017**, *64*, 2608–2619. [CrossRef]

36. Zhang, L.; Shi, D.; Yang, T.; Wang, K.; Tang, Y.; Loh, W.K. Partial Power Processing for Power Decoupling Network in Three-Phase Three-Leg Four-Wire Three-Level T-Type Inverter with Reduced Split DC-Bus Capacitance. *IEEE Trans. Ind. Electron.* **2021**. [CrossRef]

37. Salmon, J. Comparative Evaluation of Circuit Topologies for 1-Phase and 3-Phase Boost Rectifiers Operated with a Low Current Distortion. In Proceedings of the 1994 Proceedings of Canadian Conference on Electrical and Computer Engineering (CCECE), Halifax, NS, Canada, 25–28 September 1994; Volume 1, pp. 30–33. [CrossRef]

38. Dahono, P.; Sato, Y.; Kataoka, T. Analysis and Minimization of Ripple Components of Input Current and Voltage of PWM Inverters. *IEEE Trans. Ind. Appl.* **1996**, *32*, 945–950. [CrossRef]

39. Cittanti, D.; Mandrile, F.; Gregorio, M.; Bojoi, R. Design Space Optimization of a Three-Phase LCL Filter for Electric Vehicle Ultra-Fast Battery Charging. *Energies* **2021**, *14*, 1303. [CrossRef]

40. Magnetics. 00X6527E060 Datasheet. Available online: https://www.mag-inc.com/Products/Powder-Cores/XFlux-Cores (accessed on 11 May 2021).

41. Borlo, S.; Cittanti, D.; Gregorio, M.; Mandrile, F.; Musumeci, S. Comparative CCM-DCM Design Evaluation of Power Inductors in Interleaved PFC Stage for Electric Vehicle Battery Chargers. In Proceedings of the International Conference on Clean Electrical Power (ICCEP), Otranto, Italy, 2–4 July 2019; pp. 180–186. [CrossRef]

42. Liserre, M.; Dell'Aquila, A.; Blaabjerg, F. Stability Improvements of an LCL-Filter Based Three-Phase Active Rectifier. In Proceedings of the IEEE Power Electronics Specialists Conference (PESC), Cairns, QLD, Australia, 23–27 June 2002; Volume 3, pp. 1195–1201. [CrossRef]

43. Hoevenaars, T.; LeDoux, K.; Colosino, M. Interpreting IEEE STD 519 and Meeting its Harmonic Limits in VFD Applications. In Proceedings of the IEEE Petroleum and Chemical Industry Conference (PCIC), Houston, TX, USA, 15–17 September 2003; pp. 145–150. [CrossRef]

44. IEEE. *IEEE Recommended Practice and Requirements for Harmonic Control in Electric Power Systems*; IEEE Std 519-2014; IEEE: Piscataway, NJ, USA, 2014; pp. 1–29. [CrossRef]

45. Blasko, V.; Kaura, V. A Novel Control to Actively Damp Resonance in Input LC Filter of a Three-Phase Voltage Source Converter. *IEEE Trans. Ind. Appl.* **1997**, *33*, 542–550. [CrossRef]

46. Jalili, K.; Bernet, S. Design of LCL Filters of Active-Front-End Two-Level Voltage-Source Converters. *IEEE Trans. Ind. Electron.* **2009**, *56*, 1674–1689. [CrossRef]

47. Cittanti, D.; Gregorio, M.; Bojoi, R. Digital Multi-Loop Control of a 3-Level Rectifier for Electric Vehicle Ultra-Fast Battery Chargers. In Proceedings of the AEIT International Annual Conference (AEIT), Catania, Italy, 23–25 September 2020. [CrossRef]

48. Blaabjerg, F.; Teodorescu, R.; Liserre, M.; Timbus, A. Overview of Control and Grid Synchronization for Distributed Power Generation Systems. *IEEE Trans. Ind. Electron.* **2006**, *53*, 1398–1409. [CrossRef]

49. Limongi, L.R.; Bojoi, R.; Pica, C.; Profumo, F.; Tenconi, A. Analysis and Comparison of Phase Locked Loop Techniques for Grid Utility Applications. In Proceedings of the Power Conversion Conference (PCC), Nagoya, Japan, 2–5 April 2007; pp. 674–681. [CrossRef]

50. Cittanti, D.; Gregorio, M.; Mandrile, F.; Bojoi, R. Full Digital Control of an All-Si On-Board Charger Operating in Discontinuous Conduction Mode. *Electronics* **2021**, *10*, 203. [CrossRef]

51. Bel Haj Youssef, N.; Al-Haddad, K.; Kanaan, H.Y. Implementation of a New Linear Control Technique Based on Experimentally Validated Small-Signal Model of Three-Phase Three-Level Boost-Type Vienna Rectifier. *IEEE Trans. Ind. Electron.* **2008**, *55*, 1666–1676. [CrossRef]

52. ST Microelectronics. STM32G474VE Datasheet. Available online: https://www.st.com/en/microcontrollers-microprocessors (accessed on 11 May 2021).

53. Dalessandro, L.; Round, S.D.; Drofenik, U.; Kolar, J.W. Discontinuous Space-Vector Modulation for Three-Level PWM Rectifiers. *IEEE Trans. Power Electron.* **2008**, *23*, 530–542. [CrossRef]43–560. [CrossRef]